Geophysical Journal International

Geophys. J. Int. (2014) **199**, 1682–1697 doi: 10.1093/gji/ggu332
GJI Seismology

Determination of elastic anisotropy of rocks from *P*- and *S*-wave velocities: numerical modelling and lab measurements

Tomáš Svitek,[1,2] Václav Vavryčuk,[3] Tomáš Lokajíček[2] and Matěj Petružálek[1,2]

[1] *Faculty of Science, Charles University in Prague, Albertov* 6, 128 43 *Praha, Czech Republic*
[2] *Institute of Geology, Academy of Sciences, Rozvojová* 269, 165 00 *Praha, Czech Republic*
[3] *Institute of Geophysics, Academy of Sciences, Boční* II/1401, 141 00 *Praha, Czech Republic. E-mail:* vv@ig.cas.cz

Accepted 2014 August 29. Received 2014 August 13; in original form 2014 February 16

SUMMARY

The most common type of waves used for probing anisotropy of rocks in laboratory is the direct *P* wave. Information potential of the measured *P*-wave velocity, however, is limited. In rocks displaying weak triclinic anisotropy, the *P*-wave velocity depends just on 15 linear combinations of 21 elastic parameters, called the weak-anisotropy parameters. In strong triclinic anisotropy, the *P*-wave velocity depends on the whole set of 21 elastic parameters, but inversion for six of them is ill-conditioned and these parameters are retrieved with a low accuracy. Therefore, in order to retrieve the complete elastic tensor accurately, velocities of *S* waves must also be measured and inverted. For this purpose, we developed a lab facility which allows the *P*- and *S*-wave ultrasonic sounding of spherical rock samples in 132 directions distributed regularly over the sphere. The velocities are measured using a pair of *P*-wave sensors with the transmitter and receiver polarized along the radial direction and using two pairs of *S*-wave sensors with the transmitter and receiver polarized tangentially to the spherical sample in mutually perpendicular directions. We present inversion methods of phase and ray velocities for elastic parameters describing general triclinic anisotropy. We demonstrate on synthetic tests that the inversion becomes more robust and stable if the *S*-wave velocities are included. This applies even to the case when the velocity of the *S* waves is measured in a limited number of directions and with a significantly lower accuracy than that of the *P* wave. Finally, we analyse velocities measured on a rock sample from the Outokumpu deep drill hole, Finland. We present complete sets of elastic parameters of the sample including the error analysis for several levels of confining pressure ranging from 0.1 to 70 MPa.

Key words: Geomechanics; Microstructures; Body waves; Seismic anisotropy; Wave propagation; Acoustic properties.

1 INTRODUCTION

Laboratory measurements as well as in situ observations confirm that majority of real rocks are anisotropic. Elastic anisotropy can be intrinsic if formed by anisotropic mineral grains, but also effective if produced by the presence of layers, preferentially oriented small scale inhomogeneities or joints, cracks and microcraks. Intrinsic rock anisotropy origins either in the preferential arrangement of anisotropic mineral grains being called the 'lattice-preferred orientation (LPO)' anisotropy or 'crystallographic-preferred orientation (CPO)' anisotropy (Karato 2008), or it can origin in a shape predisposition of individual mineral grains being called the 'shape-preferred orientation (SPO)' anisotropy (Mainprice & Nicolas 1989; Ildefonse *et al.* 1992; Kitamura 2006; Valcke *et al.* 2006). Anisotropy of a rock is very often produced by defects such as cracks, microcracks or pores created during tectonic evolution of the rock when exposed to temperature–pressure conditions of a surrounding environment. Consequently, rock is damaged and becomes full of systems of pervasive cracks or microcracks of various scales and orientations (Sayers & Kachanov 1995; Dewhurst & Siggins 2006; Kern *et al.* 2008). Parameters of anisotropy depend also on whether or not and what content saturates the free space of these defects (Hornby 1998; Sayers 2002; Piane *et al.* 2011; Wang *et al.* 2012).

Anisotropic properties of rocks can be measured in laboratory on rock samples or in situ. The laboratory methods are, for example, the microscopic image analyses, ultrasonic sounding, neutron diffraction (Xie *et al.* 2003; Nikitin & Ivankina 2004; Ivankina *et al.* 2005), static and dynamic loading tests in pressure or tense regimes. In *in situ* conditions like in gas and oil reservoirs, anisotropy of rocks is measured by the multi-offset multi-azimuthal vertical seismic profiling (Okaya *et al.* 2004; Asgharzadeh *et al.* 2013) or by the shear-wave splitting analysis (Crampin 1985; Savage 1999; Peng & Ben-Zion 2004). In general, acoustic and/or seismic methods are based mainly on the determination of the traveltime of elastic waves, well known as the 'time-of-flight' measurements. As we know the distance between the source and a receiver, it is possible to determine the propagation velocity of individual waves in the respective propagation direction and consequently to invert the directionally dependent velocity for anisotropic parameters.

The most common type of waves used for probing anisotropy of rocks in the laboratory is the direct *P* wave (Christensen 1966; Pros *et al.* 1998; Bóna *et al.* 2012; Lokajíček *et al.* 2013). This wave can easily be generated and recorded, and its interpretation is simpler than that of waves coming at later times including the *S* waves. The information potential of the measured *P*-wave velocity, however, is limited. In rocks displaying weak triclinic anisotropy, the *P*-wave velocity depends just on 15 linear combinations of 21 elastic parameters, called the weak-anisotropy parameters (Mensch & Rasolofosaon 1997; Pšenčík & Gajewski 1998; Vavryčuk 2009). The remaining elastic parameters cannot be retrieved. In strong triclinic anisotropy, the *P*-wave velocity depends on all 21 elastic parameters, but inversion for six of them is ill-conditioned and these parameters are retrieved with a low resolution. This deficiency can be removed only by incorporating the *S*-wave velocities. The measurement of the *S*-wave velocities is, however, more difficult; it requires equipping special transmitters and sensors for generating and recording the *S* waves, and the interpretation of recorded signals is also more involved (Kern 1982; Siegesmund *et al.* 1991).

In this paper, we present an approach of measuring the *P*- and *S*-wave velocities on rock samples and inverting them for elastic anisotropy. In order to be able to analyse a general anisotropy of no symmetry, we developed a new high pressure apparatus that allows measuring the *P*- and *S*-wave velocities on spherical rock samples. The velocities are measured in 132 independent directions which provide good spatial coverage (Pros *et al.* 1998) needed for a reliable determination of anisotropy parameters. The waveforms are recorded with radial as well as two mutually perpendicular transverse sensors in order to identify the two *S* waves and to measure their arrivals accurately. We present inversion schemes for determining anisotropy parameters using phase as well as ray velocities and test their robustness on synthetic models. We show how the accuracy of the parameters is improved if the *S*-wave measurements are incorporated. Finally, we exemplify our approach on real measurements obtained for a strongly foliated fine-grained biotite gneiss from the Outokumpu deep drill hole, Finland (Kern *et al.* 2009) exposed to various confining pressure conditions.

2 THEORY

2.1 Determination of anisotropy from phase velocities

The phase velocity describes the propagation of plane waves and is directed along the phase normal (i.e. the normal to the wave front). The phase velocity of plane waves propagating in a homogeneous anisotropic medium is described by the Christoffel equation (Musgrave 1970; Helbig 1994):

$$\det\left(\Gamma_{ij} - c^2\delta_{ij}\right) = 0, \tag{1}$$

where c is the phase velocity of the *P*, *S*1 or *S*2 waves, δ_{ij} is the Kronecker delta and Γ_{ij} is the Christoffel tensor,

$$\Gamma_{jk} = a_{ijkl}n_i n_l. \tag{2}$$

Parameters a_{ijkl} are the components of the elastic (stiffness) tensor normalized to density, and vector $\mathbf{n}$ is the phase normal. If elastic parameters a_{ijkl} are known, eq. (1) is the cubic equation for the squared phase velocity c. If the phase velocity c is known from measurements, eq. (1) defines an inverse problem for calculating elastic parameters a_{ijkl}. This inversion is non-linear and usually solved by iterations using perturbation theory (Klíma 1973; Jech & Pšenčík 1989; Jech 1991; Vavryčuk 2013).

In perturbation theory, we assume that the anisotropic medium defined by unknown parameters a_{ijkl} can be obtained by a small perturbation of a known reference medium

$$a_{ijkl} = a^0_{ijkl} + \Delta a_{ijkl}, \tag{3}$$

where a^0_{ijkl} defines the reference medium and Δa_{ijkl} its perturbation. Under this assumption, the cubic equation for phase velocity c can be linearized as follows (Jech & Pšenčík 1989; Pšenčík & Vavryčuk 2002):

$$\Delta(c^2) = \Delta a_{ijkl}n_i n_l g^0_j g^0_k, \tag{4}$$

where $\mathbf{g}^0$ defines the polarization vector of the analysed wave in the reference medium, $\Delta(c^2)$ is the misfit between the measured velocity in the studied anisotropic medium and the velocity in the reference medium. Eq. (4) represents a system of linear equations for unknown perturbations, Δa_{ijkl}, which can be solved in iterations. In the first iteration, the reference medium is assumed to be isotropic. Its *P*- and *S*-wave velocities can be obtained by averaging the observed directionally dependent velocities over all directions. If only *P*-wave velocities are measured and inverted, a rough estimate of the *S*-wave velocity in the isotropic reference medium must also be supplied. We can use, for example, a value obtained from the Poisson ratio between the *P* and *S* velocities, $V_S = V_P/\sqrt{3}$. In higher iterations, the reference medium is the result of the previous iteration.

Using the above approach, we can invert for all of 21 elastic parameters. However, not all of them are retrieved with the same accuracy. In the case of the *P*-wave velocity inversion, 15 parameters are well resolved but six parameters related to the *S*-wave propagation (hereafter the *S*-wave related parameters) a_{44}, a_{55}, a_{66}, a_{45}, a_{46} and a_{56} are less accurate. Under weak anisotropy, these six parameters cannot be determined from the *P*-wave velocities at all. Hence, in order to determine the complete elastic tensor accurately, measurements of the *S*-wave velocities must be utilized in the inversion.

2.2 Determination of anisotropy from ray velocities

The ray velocity defines the signal propagation and energy transport and is directed along a ray. If anisotropy under study is weak, we do not need to distinguish between the phase and ray velocities. Their magnitudes are approximately equal and directions differ by a small angle (Vavryčuk 1997; Pšenčík & Vavryčuk 2002; Farra 2004). However, if anisotropy is strong, the phase and ray velocities are different. For this reason, it is important to understand which velocity is measured in the field or lab experiments. If the waves used for determining anisotropy are generated by point sources, the ray velocity is usually measured and the procedure of the inversion for elastic anisotropy described in Section 2.1 must be modified.

The ray velocity vector **v** is defined as (Červený 2001, his eq. 2.4.46):

$$v_i = vN_i = a_{ijkl}p_l g_j g_k, \tag{5}$$

where v is the ray velocity, **N** is the ray direction, a_{ijkl} are the density-normalized elastic parameters, $\mathbf{p} = \mathbf{n}/c$ is the slowness vector, **n** is the phase normal, $c = 1/p$ is the phase velocity, p is the slowness and **g** is the polarization vector. Vectors **v** and **p** are related by the following equation,

$$\mathbf{v} \cdot \mathbf{p} = 1 \tag{6}$$

expressing the polar reciprocity of the slowness and wave surfaces (Helbig 1994). This condition means that vector **v** is normal to the slowness surface $p = p(\mathbf{n})$ and vector **p** is normal to the wave surface $v = v(\mathbf{N})$. Hence, if ray velocity v is measured in a sufficiently dense grid of ray directions **N**, we can calculate vectors **n** as normals to the wave surface using standard formulae of differential geometry (Lipschutz 1969). Subsequently, phase velocity c can be calculated for vectors **n** using the following formula

$$c = vN_i n_i. \tag{7}$$

Having computed $c = c(\mathbf{n})$ we can invert for anisotropic parameters using the procedure described in Section 2.1. Obviously, if we combine several types of waves in the inversion, which were measured for the same set of ray directions **N**, the sets of phase normals **n** are different for individual wave types.

It should be noted that the above approach has some limitations. The geometry of the wave surface can be much more complicated than that of the slowness or phase velocity surface (Musgrave 1970). For *S* waves, the wave surface can be multivalued with triplications and cusp edges (Vavryčuk 2006). In general, the complexity of the wave surface increases with strength of anisotropy. So, it can happen under strong anisotropy that the complete slowness or phase velocity surface can be constructed only using velocity measurements on a very fine grid of ray directions and by identifying and interpreting also later arrivals of waves. If the wave surface of *S* waves is extremely complicated, we can avoid problems with the triplications and the cusp edges by calculating the wave normals (and corresponding phase velocities) only for smooth parts of the wave surface. In this way, we will not be able to reconstruct the complete slowness or phase velocity surfaces of the *S* waves but only their isolated patches. Fortunately, this is not critical for the inversion for anisotropic parameters. As will be shown in synthetic tests, the inversion can work robustly even when measurements of the *P*-wave velocities are supplemented by a limited number of measurements of the *S*-wave velocities.

The above approach is advantageous, because it is a simple generalization of the inversion of the phase velocities described in Section 2.1. First, we pre-process the input data by transforming the ray velocities to the phase velocities, and then we apply the standard inversion scheme. However, anisotropic parameters can also be calculated using other approaches, for example, if ray velocities are measured together with polarization vectors (Bóna *et al.* 2008).

3 SYNTHETIC TESTS

In this section, the robustness of the inversion of phase velocities for elastic anisotropy is studied using numerical modelling. For synthetic anisotropy, we adopted elastic parameters of quartz published

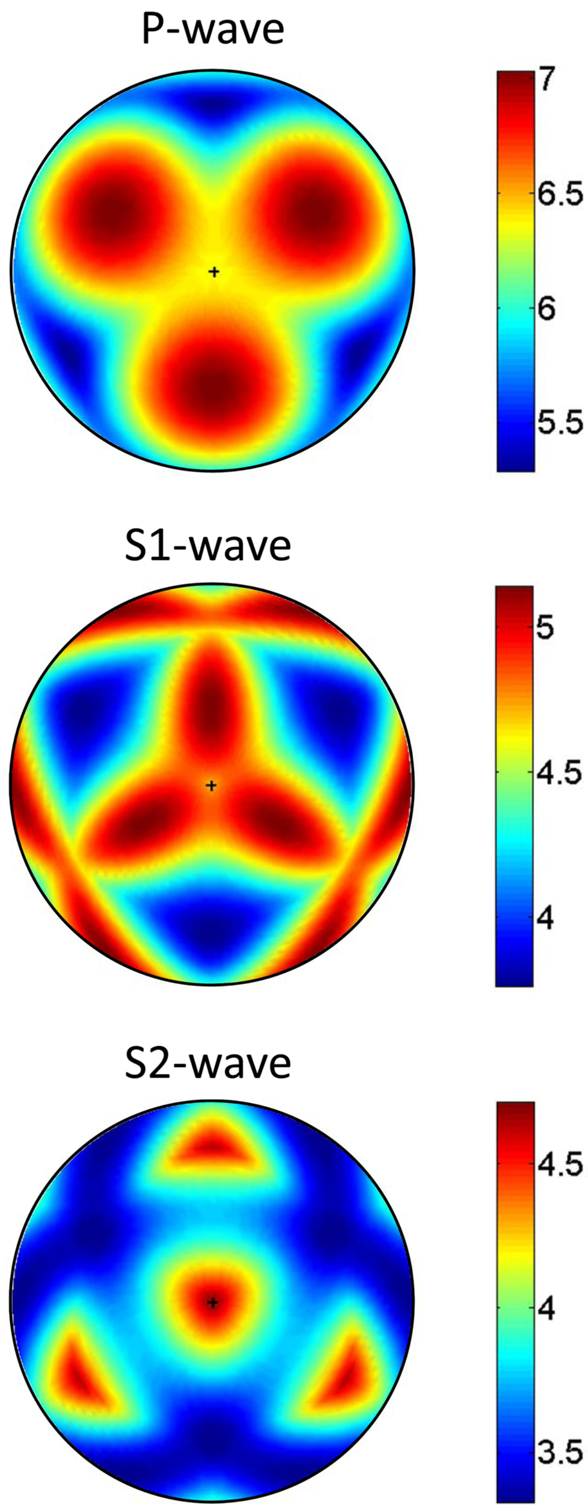

Figure 1. The *P*-, *S*1- and *S*2-wave phase velocities of anisotropy used in the synthetic tests. The colour-coded velocities are in km s^{-1}.

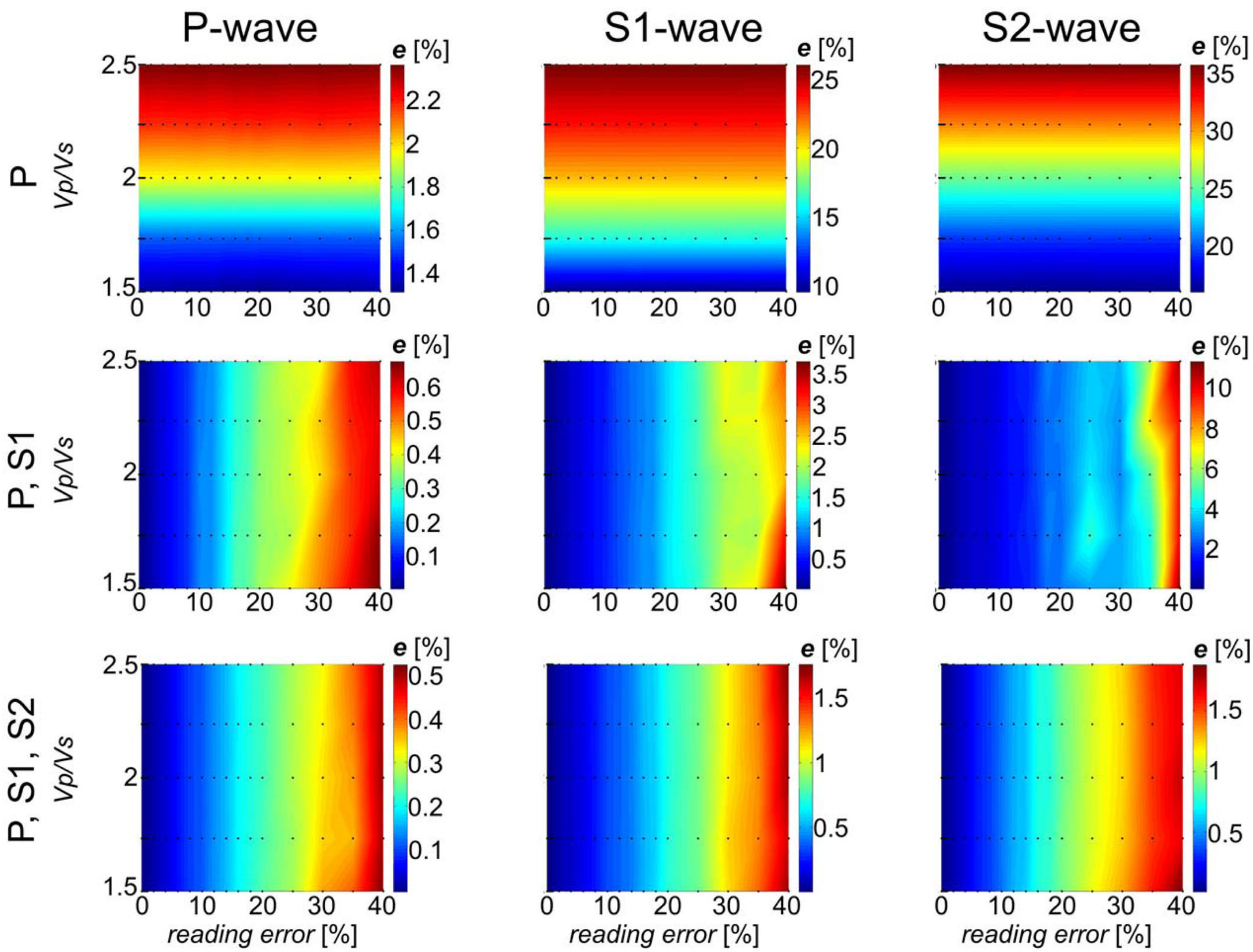

Figure 2. Error e_{mean} of the predicted *P*-wave (left-hand panel), *S*1-wave (middle panel) and *S*2-wave (right-hand panel) velocities as a function of the reading error of the measured *S*1-wave velocities (middle row) and *S*1- and *S*2-wave velocities (bottom row). The inversion is performed using velocities measured in all 132 directions. The errors in the top row panels are independent of the reading error of the *S*-wave velocities, because only the *P*-wave velocities are inverted. The dots indicate points in which error e_{mean} is calculated.

by Klíma (1973):

$$C_{ij}^{\mathrm{quartz}} = \begin{bmatrix} 86.05 & 4.85 & 10.45 & 18.25 & 0 & 0 \\ 4.85 & 86.05 & 10.45 & -18.25 & 0 & 0 \\ 10.45 & 10.45 & 107.1 & 0 & 0 & 0 \\ 18.25 & -18.25 & 0 & 58.65 & 0 & 0 \\ 0 & 0 & 0 & 0 & 58.65 & 18.25 \\ 0 & 0 & 0 & 0 & 18.25 & 40.60 \end{bmatrix}. \tag{8}$$

The values in eq. (8) are in GPa and the density of quartz is $\rho = 2.65$ g cm^{-3}. Anisotropy displays a trigonal symmetry. Strength of the *P*-, *S*1- and *S*2-wave anisotropy is 26.6, 29.9 and 27.8 per cent, respectively. For the directional variation of the *P*-, *S*1- and *S*2-wave phase velocities, see Fig. 1. The velocities used in the inversion are calculated in a regular grid of directions with latitude ranging from –75° to 75° in step of 15° and longitude from 0° to 360° in step of 15°. This represents a set of 132 independent directions covering the whole sphere surface.

3.1 Test 1

In this test, we study the robustness of the inversion with respect to the following factors: (1) starting model, that is the estimate of the *S*-wave velocity of the isotropic reference medium needed in the first iteration, (2) noise in input data (i.e. in the measured velocities) and (3) types of waves used in the inversion. The *S*-wave velocity of the isotropic reference model is defined by the $V_{\mathrm{P}}/V_{\mathrm{S}}$ ratio ranging from 1.5 to 2.5. The errors of the phase velocities are assumed to be 0.1 per cent at most for the *P* wave. The errors of the *S*1-wave velocities are assumed to achieve values: 0, 0.2, 0.4, 0.6, 0.8, 1, 2, 4, 6, 8, 10, 12, 14, 16, 18, 20, 25, 30, 35 and 40 per cent. The errors of the *S*2-wave velocities are 1.5 times larger than those for the *S*1 wave. A uniform random distribution was chosen for all noise levels. Every noise value was generated 100 times to get statistically relevant results. The limits of noise selected for the *P*, *S*1 and *S*2 waves are based on the analysis of real data presented in Section 4. The accuracy of the *P*-wave velocity is very high, because the *P* wave has a sharp onset with no noise before its arrival and thus picking of arrival times is quite accurate. A significantly lower accuracy of the *S*1 and *S*2 waves originates in the fact that the *S* waveforms are generally more complex and their interpretation

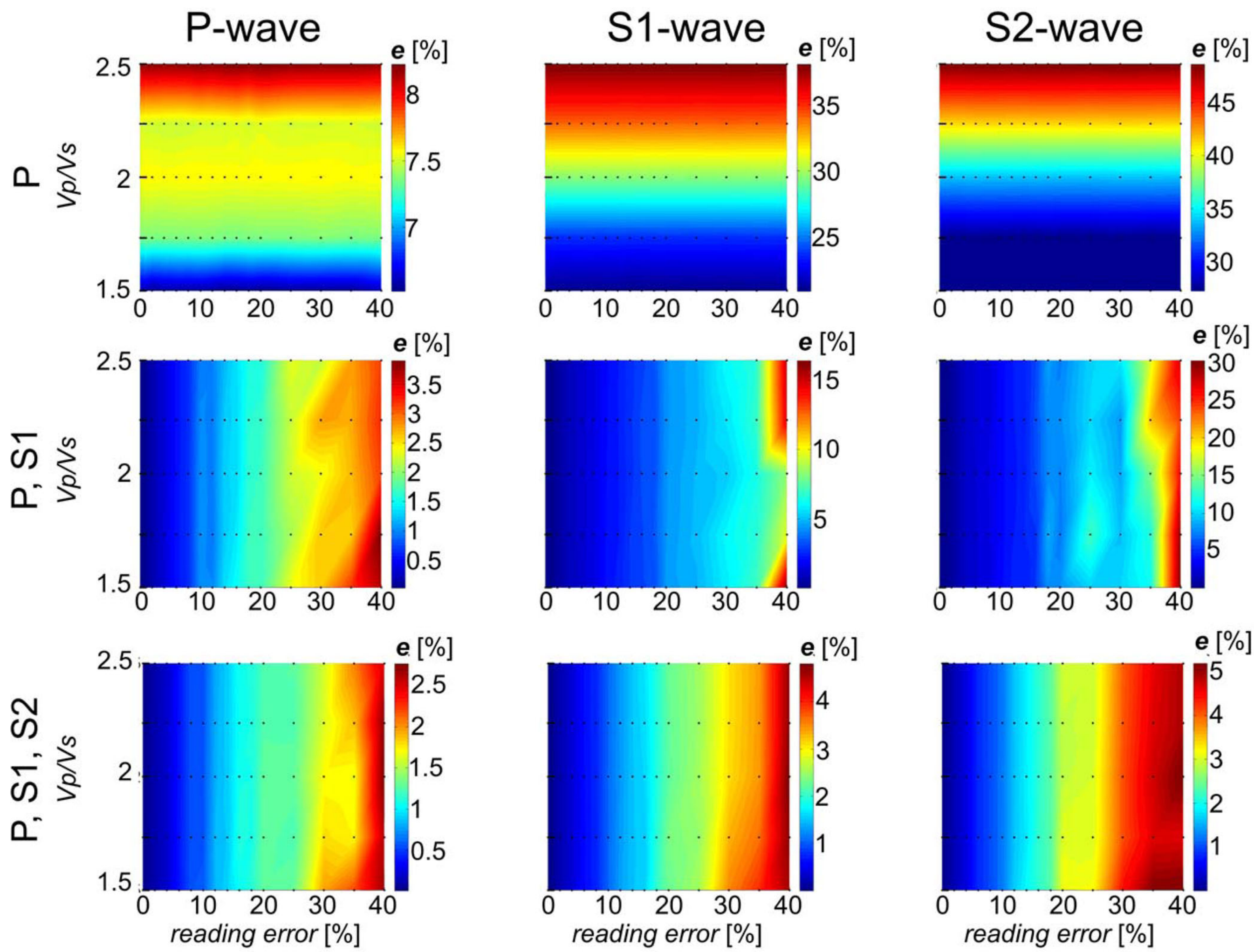

Figure 3. Error $e_{\max}$ of the predicted *P*-wave (left-hand panel), *S*1-wave (middle panel) and *S*2-wave (right-hand panel) velocities as a function of the reading error of the measured *S*1-wave velocities (middle row) and *S*1- and *S*2-wave velocities (bottom row). The inversion is performed using velocities measured in all 132 directions. The errors shown in the top row panels are independent of the reading error of the *S*-wave velocities because only the *P*-wave velocities are inverted. The dots indicate points in which error $e_{\max}$ is calculated.

is often difficult. Moreover, in the case of weak anisotropy, the two *S* waves need not be well separated; they can interfere and their reliable distinguishing is not always possible. This particularly complicates identifying the slow *S* wave. Therefore, the slow *S*-wave velocity is assumed to have systematically higher errors than the fast *S*-wave velocity. Finally, we studied the robustness of the inversion for three different input data sets. We tested inversion for anisotropy using the *P*-wave velocities only, the *P*- and *S*1-wave velocities, and the *P*-, *S*1- and *S*2-wave velocities. The success of the inversion is quantified by a relative difference between true and predicted velocities:

$$e_{\mathrm{mean}}^{P,S1,S2} = 100 \text{ per cent} \cdot \mathrm{mean}\left(\frac{\left|c_{\mathrm{true}}^{P,S1,S2} - c_{\mathrm{predicted}}^{P,S1,S2}\right|}{c_{\mathrm{true}}^{P,S1,S2}}\right),$$

$$e_{\max}^{P,S1,S2} = 100 \text{ per cent} \cdot \max\left(\frac{\left|c_{\mathrm{true}}^{P,S1,S2} - c_{\mathrm{predicted}}^{P,S1,S2}\right|}{c_{\mathrm{true}}^{P,S1,S2}}\right), \quad (9)$$

where the predicted velocity is calculated from the retrieved anisotropic parameters. These quantities are averaged over all directions and over 100 realizations of random noise.

The results of the synthetic tests are shown in Figs 2–4. According to the results we arrive at the following conclusions:

(1) The elastic tensor computed from the *P*-wave velocities only (top rows in Figs 2 and 3) strongly depends on the $V_{\mathrm{P}}/V_{\mathrm{S}}$ ratio supplied in the first iteration. The predicted velocities of the *S*1 and *S*2 waves have significantly higher errors than those for the *P* wave. The mean errors for the *S*1 and *S*2 waves are about 10 and 15 times higher than for the *P* waves, respectively. Thus the *S*-wave related parameters cannot be reliably retrieved even if the accuracy of the *P*-wave velocities is quite high (0.1 per cent at most). Consequently, the *S*1- and *S*2-wave velocities calculated from the retrieved elastic tensor are highly inaccurate.

(2) The elastic tensor computed from the *P*- and *S*1-wave velocities (middle rows in Figs 2 and 3) is insensitive to the $V_{\mathrm{P}}/V_{\mathrm{S}}$ ratio supplied in the first iteration. The accuracy of the predicted velocities depends on the picking accuracy of the *S*1-wave onsets. Interestingly, including quite inaccurate measurements of the *S*-wave velocities still improves the accuracy of the elastic tensor (Fig. 4, bottom row). Even the fit between the predicted and true *P*-wave velocities is better. If the *S*1-wave velocities are measured with the mean errors less than

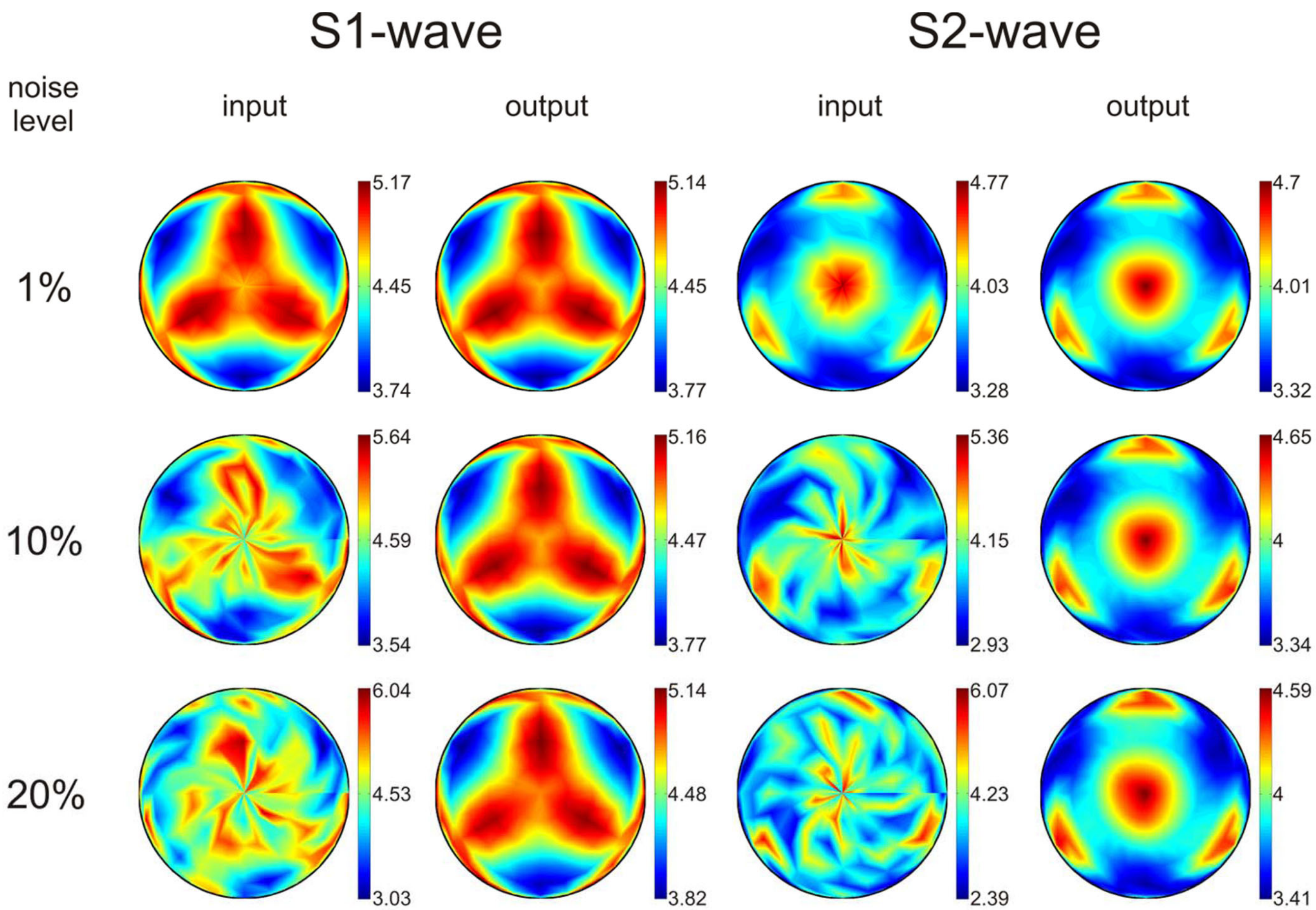

Figure 4. Examples of input noisy $S1$- and $S2$-wave velocities used in the inversion and the corresponding output velocities predicted from the retrieved elastic parameters. The noise levels of the $S1$-wave velocities are: 1 per cent (top row), 10 per cent (middle row) and 20 per cent (bottom row), respectively. The colour-coded velocities are in km s^{-1}. The figure demonstrates that the inversion is robust and stable even for a high level of noise.

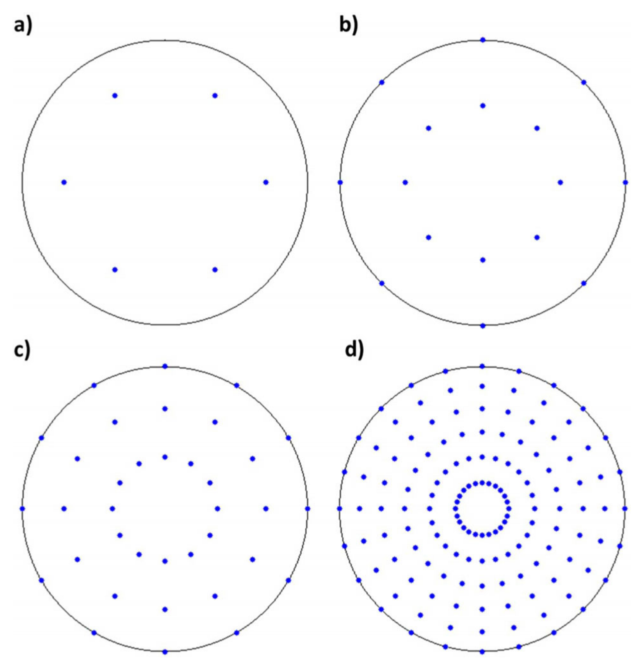

Figure 5. The stereographic projection of directions with velocity measurements used in the synthetic tests: the regular grid of (a) 6 directions (60° step), (b) 12 directions (45° step), (c) 30 directions (30° step) and (d) 132 directions (15° step).

15 per cent, the mean errors of the predicted P-, $S1$- and $S2$-wave velocities are less than 0.3, 1 and 3 per cent, respectively.

(3) The elastic tensor computed from the P-, $S1$- and $S2$-wave velocities (bottom rows in Figs 2 and 3) is mainly dependent on the accuracy of the inverted $S1$- and $S2$-wave velocities. The additional information on the $S2$-wave velocities improves the accuracy of the predicted $S1$- and $S2$-wave velocities. The accuracy of the P-wave velocities is not further improved.

In summary, the performed synthetic tests indicate that the components of the elastic tensor inverted from the P-wave velocities only are determined with a reasonable accuracy except for the S-wave related parameters. These parameters should be viewed as very approximate and rather unreliable. The complete elastic tensor characterizing trigonal (or more general) anisotropy can be computed only when including the S-wave velocities into the inversion. Including the S-wave velocities leads to increasing the accuracy of the S-wave related parameters but also of the complete elastic tensor.

3.2 Test 2

Including information on the S-wave velocities into the inversion is not always an easy task. The S waves can be contaminated by the P-wave generated noise. Also, the two S waves do not often separate. In addition, the S waves can interfere in a complicated way near the S-wave singularities (Vavryčuk 2005a,b). In such cases, it is not

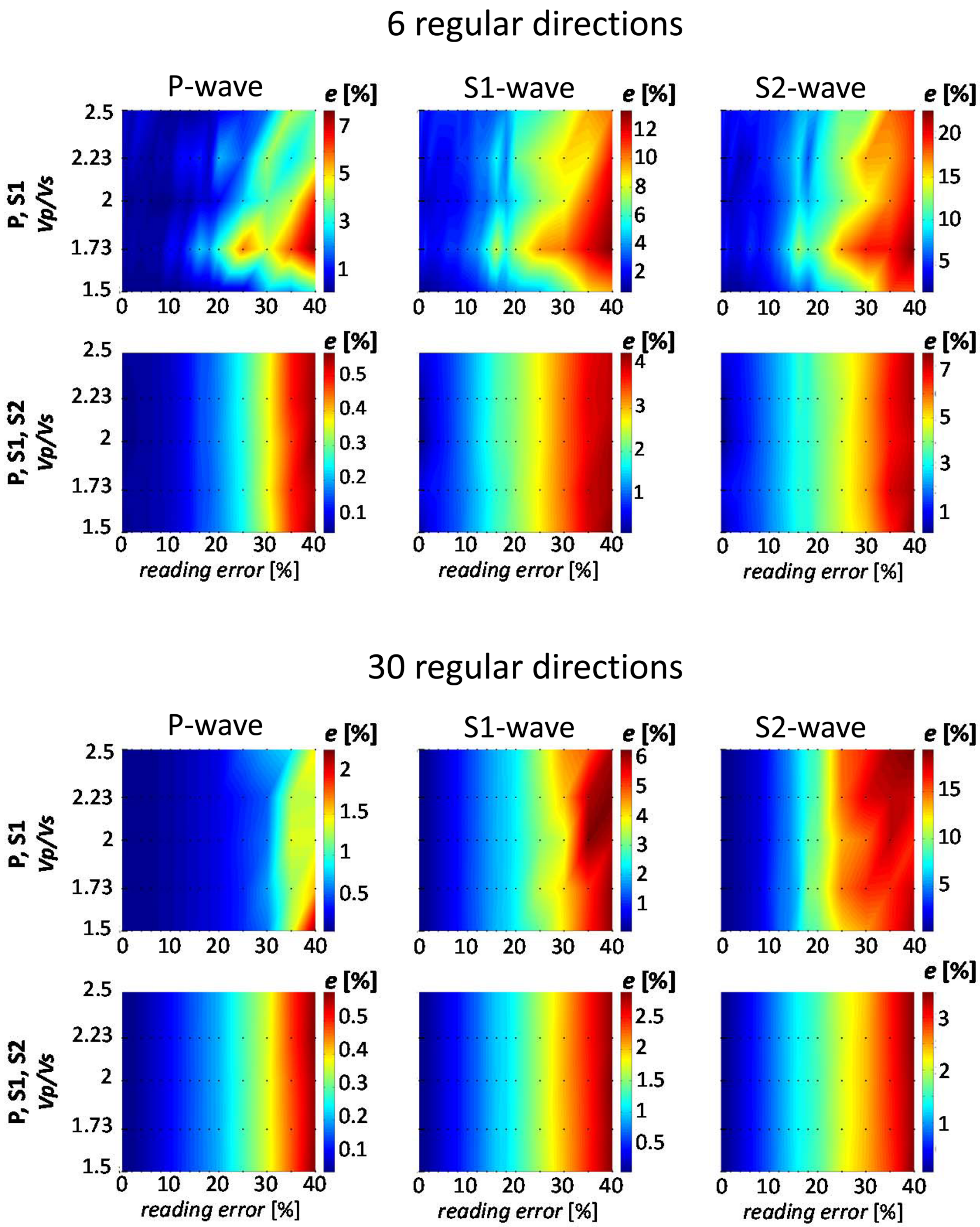

Figure 6. Error e_{mean} of the P-, $S1$- and $S2$-wave velocities as a function of the reading error of the measured $S1$-wave velocities (top row of each composite plot) and $S1$- and $S2$-wave velocities (bottom row of each composite plot). The inversion is performed using the P-wave velocities in all 132 directions and the S-wave velocities for a regular grid of six directions (upper plots) and 30 directions (lower plots). The dots indicate points in which error e_{mean} is calculated.

Table 1. Error e_{mean} as a function of the number of regular directions with the measured *S*-wave velocities used in the inversion. The *P*-wave velocities are measured in all 132 directions with error of 0.1 per cent. The errors of the measured *S*1- and *S*2-wave velocities are 40 and 60 per cent, respectively.

Error e_{mean}	*P*, *S*1 data Number of *S* directions		*P*, *S*1, *S*2 data Number of *S* directions	
	6	132	6	132
*S*1 wave	15 per cent	3.5 per cent	4.5 per cent	1.6 per cent
*S*2 wave	27 per cent	11 per cent	8 per cent	1.7 per cent

possible to measure reliably arrivals of one or both of the two *S* waves in some directions. For these reasons, we designed another synthetic test in which we analysed the accuracy of the inverted elastic tensor in dependence on the number of directions in which the *S*-wave velocities could be measured reliably.

Similarly as in Test 1, the errors were evaluated using eq. (9) being averaged over 100 realizations of random noise. The noise level of the measured *P*-wave velocity was 0.1 per cent as in Test 1. The inversion was performed with the *P*-wave velocities measured in all 132 directions (see Fig. 5d) and with the *S*-wave velocities measured in 6, 12, 30 and 132 regularly distributed directions (see Fig. 5). The accuracy of the *S*-wave velocities due to picking errors of the *S*-wave arrivals is the same as in Test 1.

The results of the test for 6 and 30 regular directions of the *S*-wave velocities are shown in Fig. 6. The errors of the inversion with the 6 and 132 regular directions of the *S*-wave velocities are summarized in Table 1. The synthetic tests indicate that including six directions with accurately measured *S*1-wave velocities is sufficient for a reliable determination of the complete elastic tensor. If the *S*1-wave velocity errors reach values of 20 per cent or more then the inversion is not improved with respect to the inversion of the

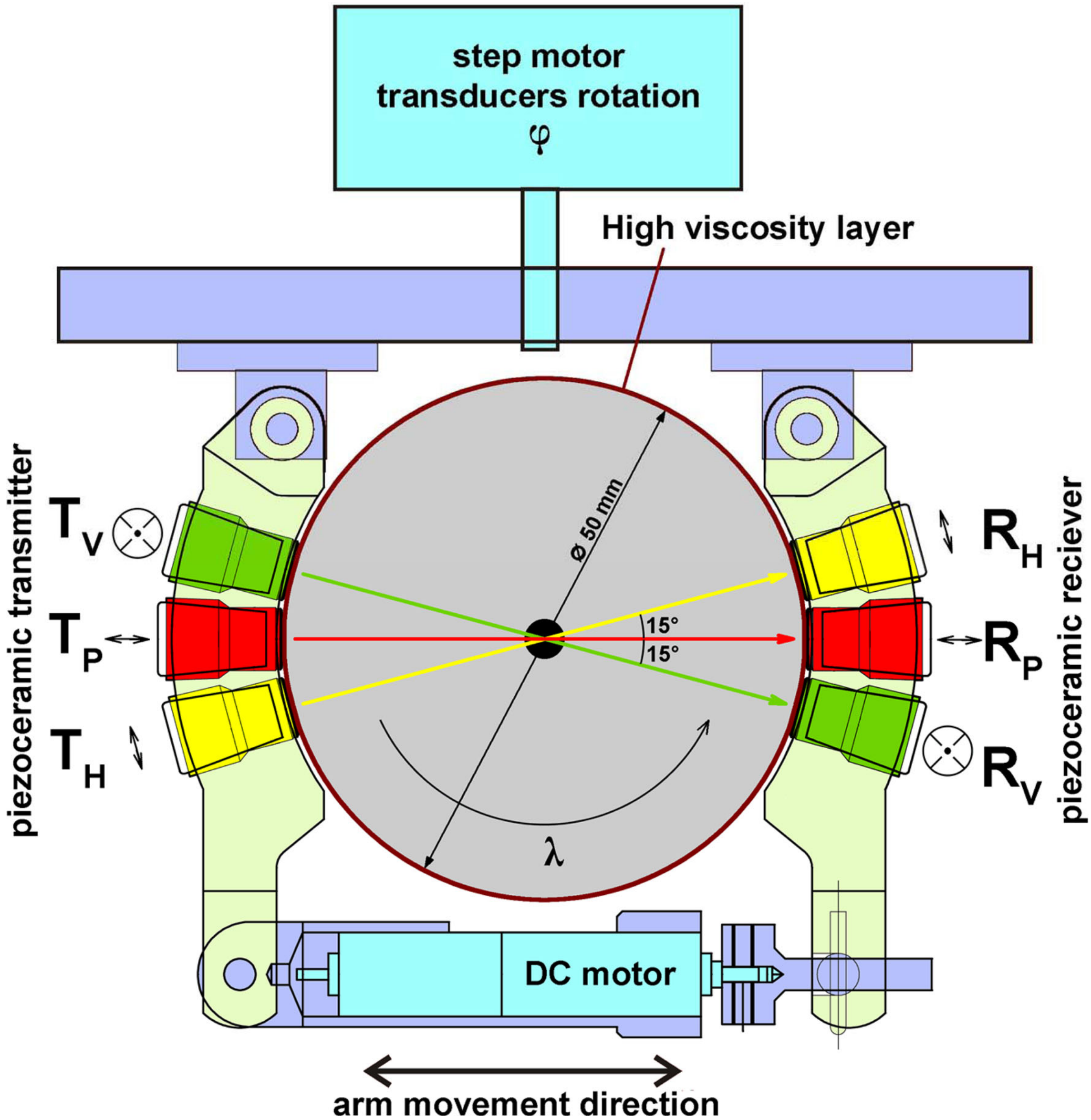

Figure 7. The experimental setup and measurement geometry; T_P and R_P are the radial transmitter and receiver, respectively (mostly generating and sensitive to the *P* waves), T_V and T_H are the transverse transmitters (mostly generating the *S* waves), and R_V and R_H are the transverse receivers (mostly sensitive to the *S* waves) lying in the vertical and horizontal planes, respectively. The axis of rotation is vertical. Modified from Lokajíček *et al.* (2014).

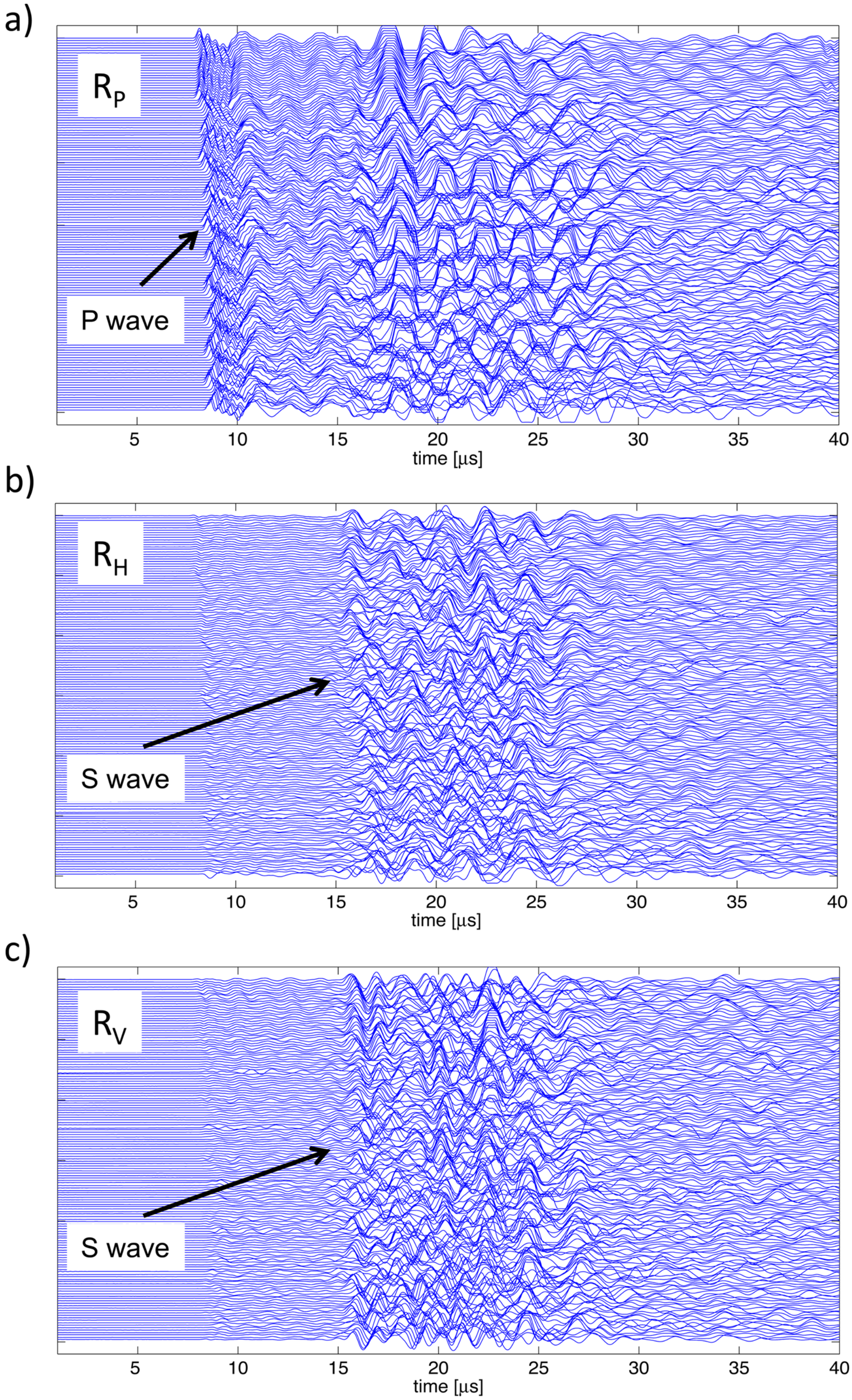

Figure 8. Waveforms of ultrasonic signals observed for the OKU-409 sample at confining pressure of 70 MPa. The waveforms are recorded in all directions at the *P*-wave sensor R_P (a), the *S*-wave sensor R_H (b) and the *S*-wave sensor R_V (c). The origin of the timescale corresponds to the excitation time of the signal.

P-wave velocities only. The results show that a much higher accuracy of the predicted *P*-wave velocities is obtained if we include the *S*2-wave velocities even for a minimum number of directions. A further increase of directions with the measured *S*2-wave velocities is not essential for improving the predicted *P*-wave velocities but significantly improves the accuracy of the predicted *S*1- and *S*2-wave velocities.

For completeness, we also performed synthetic tests with inverting the *S*-wave velocities measured in directions with an irregular distribution over the sphere. The tests revealed that the accuracy of results is two to three times lower than if the inversion is performed with a regular distribution of directions. This emphasizes the necessity of uniform coverage of the sphere by velocity measurements for the inversion to work efficiently.

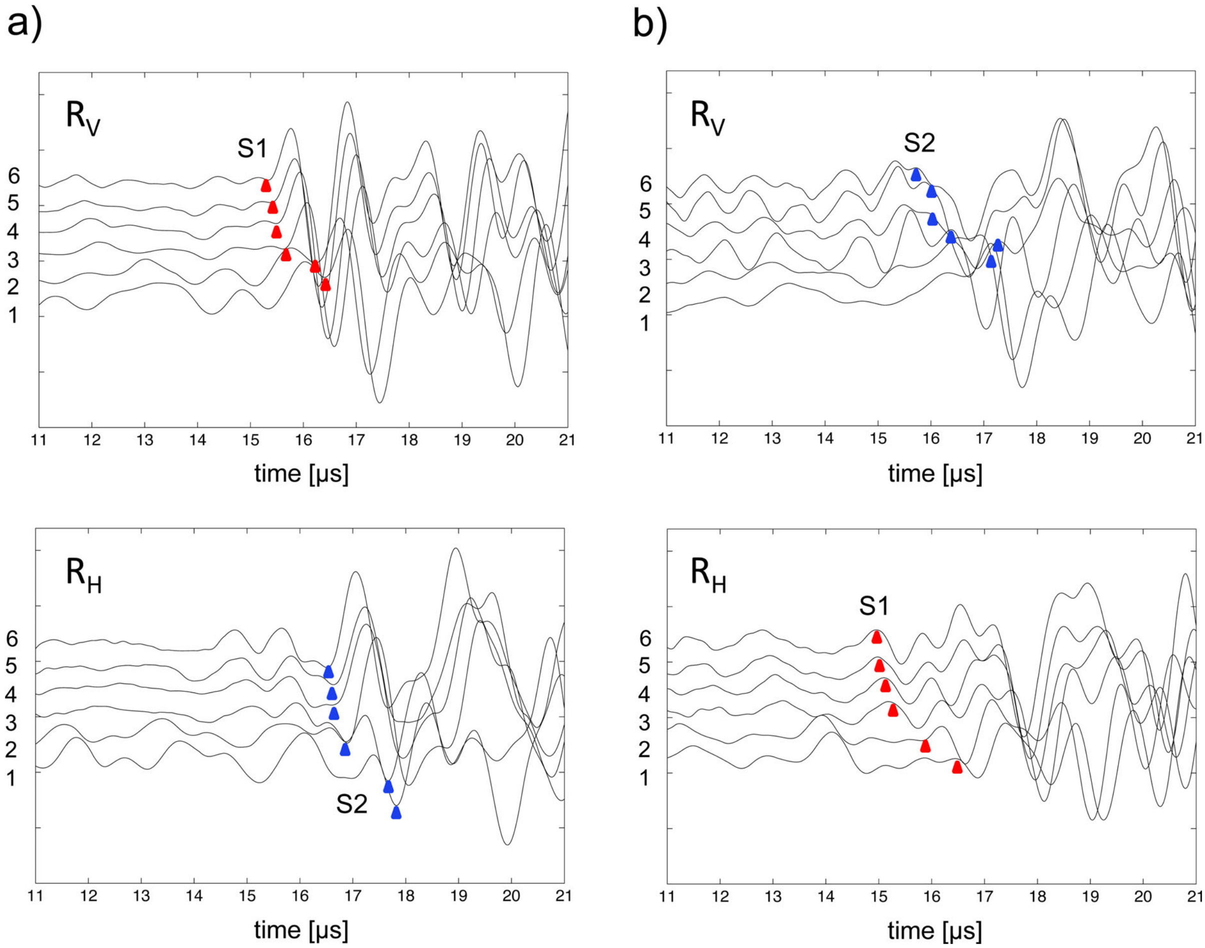

Figure 9. Examples of waveforms of ultrasonic signals observed for the OKU-409 sample on the transverse receivers: (a) waveforms in a direction in which clear *S*-wave onsets are observed, (b) waveforms in a direction in which rather unclear and disturbed *S*-wave onsets are observed. The waveforms in the individual panels are recorded under six different pressure levels with an increasing order: label 1 corresponds to 0.1 MPa, and label six corresponds to 70 MPa. The red and blue triangles mark the *S*1- and *S*2-wave arrival times, respectively. The origin of the timescale corresponds to the excitation time of the signal.

4 EXPERIMENTAL DATA

4.1 Setup of the experiment

The determination of elastic anisotropy is exemplified using an experimental facility allowing a measurement of the *P*- and *S*-wave ray velocities on spherical samples with a diameter of 50 mm. The sample was exposed to the following six confining pressure levels: 0.1, 5, 10, 20, 40 and 70 MPa. The acoustic signals are excited and recorded by three piezoceramics sensor couples with a resonant frequency of 2 MHz. The equipment allows an ultrasonic sounding of spherical rock samples in 132 independent directions by using a pair of the *P*-wave sensors (the transmitter and receiver polarized along the radial direction) and two pairs of the *S*-wave sensors (the transmitter and receiver polarized tangentially to the spherical sample, see Fig. 7). The waveforms of ultrasonic signals were recorded using an A/D convertor with the dynamic range of 8 bits and with the sampling frequency of 100 MHz. Each waveform was recorded 10 times and then averaged in order to reduce noise. The sensitivity of the convertor was set up to record individual signals without any distortion and with the maximum possible dynamics. For the *S*-wave velocity measurements, the spherical sample and contact planes of all transducers were covered by a viscous gel to allow transferring shear wave energy. Due to this gel, the sensors are not at a point contact with the sample as for the *P*-wave sensors, but may have a diameter of 1 mm or more. During the measurement, the contact between the spherical sample and the transducers was repeatedly eliminated and re-established by a miniature DC motor.

4.2 Rock sample

The measurements were performed on rock sample OKU-409 from the Outokumpu deep drill hole, Finland (Kern *et al.* 2009; Kukkonen *et al.* 2011). The sample sphere was prepared from a core segment recovered from depth of 409 m. The sample is a homogeneous biotite gneiss with pronounced foliation and lineation. The modal composition is 39.6 vol.-per cent quartz, 36.9 vol.-per cent plagioclase, 23.4 vol.-per cent biotite (Kern *et al.* 2009). The foliation and lineation are defined by platy and elongated biotite minerals exhibiting a strong shape preferred orientation. The bulk density of the rock sample as calculated from mass and dimensions of the sphere is 2.724 g cm^{-3}. Various properties of this rock as the texture pattern, the petrophysical and elastic properties have been studied and described by many authors (Kern *et al.* 2008, 2009; Elbra *et al.* 2011; Wenk *et al.* 2012). In particular, the focus was put on elastic anisotropy determined using various methods. It was measured on a spherical sample using the apparatus described in this paper, on a cube sample using a multi-anvil pressure apparatus, and it was also calculated from the texture-based data. A detailed review of the results can be found in Lokajíček *et al.* (2014).

4.3 Data processing

Processing of waveforms provides the *P*-, *S*1- and *S*2-wave onset times in 132 independent directions (see Fig. 8). Since the *P*-wave onset is usually noise-free and well distinguished, the determination of the *P*-wave arrivals is rather easy and can be performed automatically (Allen 1982; Lokajíček & Klíma 2006; Sedlák *et al.* 2009; Svitek *et al.* 2010). The *S* waveforms, however, are often complex and their arrivals can be unclear and hidden in noise. For this reason, the *S*1- and *S*2-wave arrivals were determined manually after a careful inspection of an analyst. The quality of the waveforms recorded in different directions is exemplified in Fig. 9. The figure shows that finding the onsets of the *S* waves is not always obvious. Waveforms from the vertically and horizontally polarized receivers are shown on the top and bottom of the figure, respectively. Six signals at each plot represent ultrasonic sounding in the same direction but under different confining pressures. Fig. 9(a) shows signals of a very good quality where onsets of the *S* waves can be determined quite accurately, whereas Fig. 9(b) shows signals of a worse quality. All picks were found manually. The accuracy of picking can be increased if waveforms at all pressure levels are plotted and interpreted simultaneously as shown in Fig. 9. Since the waveforms are often similar, the delay times between the *S*-wave arrivals at different pressure levels could also be determined automatically by cross-correlating the waveforms.

Under increasing confining pressure, the propagation velocities are increased but also anisotropy strength is changed. For example, strength of anisotropy is almost 21.4, 5.3 and 5.1 per cent at atmospheric pressure but only 11.2, 3.2 and 4.8 per cent at 70 MPa for the *P*, *S*1 and *S*2 waves, respectively.

4.4 Results

First, we focus on determining anisotropic parameters of the rock sample at pressure of 70 MPa. We calculate phase velocities from the measured ray velocities according to Section 2.2 and then we run the inversion of the phase velocities for anisotropic parameters according to Section 2.1.

Fig. 10 shows the predicted *P*-, *S*1- and *S*2-wave phase velocities when the elastic tensor was inverted from the *P*-wave velocities only, the *P*- and *S*1-wave velocities, and finally from the *P*-, *S*1- and *S*2-wave velocities. Interestingly, the predicted *P*-wave velocity pattern is very similar for all three data sets but the predicted *S*-wave velocity pattern is remarkably different. This applies to both *S*1 and *S*2 waves. The most accurate result is presented at the bottom row of Fig. 10 when the *P*-, *S*1- and *S*2-wave velocities have been inverted.

Second, we analyse an iteration process of the inversion. Fig. 11 shows the rms values of the *S*1- and *S*2-wave velocities through iterative cycles at three confining pressure levels: 0.1, 10 and 40 MPa.

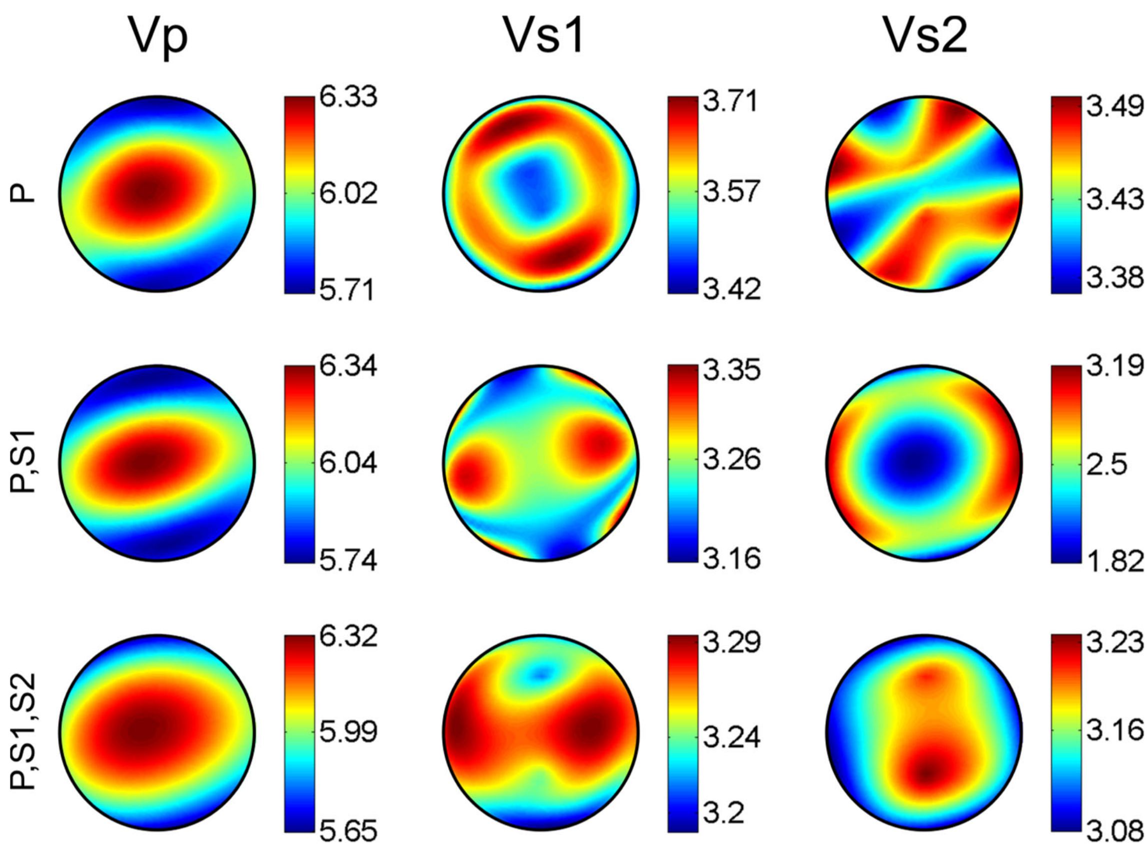

Figure 10. Phase velocities of the *P* (left-hand column), *S*1 (middle column) and *S*2 (right-hand column) waves corresponding to the elastic parameters retrieved by inverting three different data sets: the *P*-wave velocities only (top row), the *P*- and *S*1-wave velocities (middle row), and the *P*-, *S*1- and *S*2-wave velocities (bottom row). The confining pressure is 70 MPa. The colour-coded velocities are in km s^{-1}. Note a stable pattern of the *P*-wave velocities but a rather variable pattern of the *S*1- and *S*2-wave velocities, when different data sets are inverted. The most reliable and stable results are in the bottom row, where all available data are inverted.

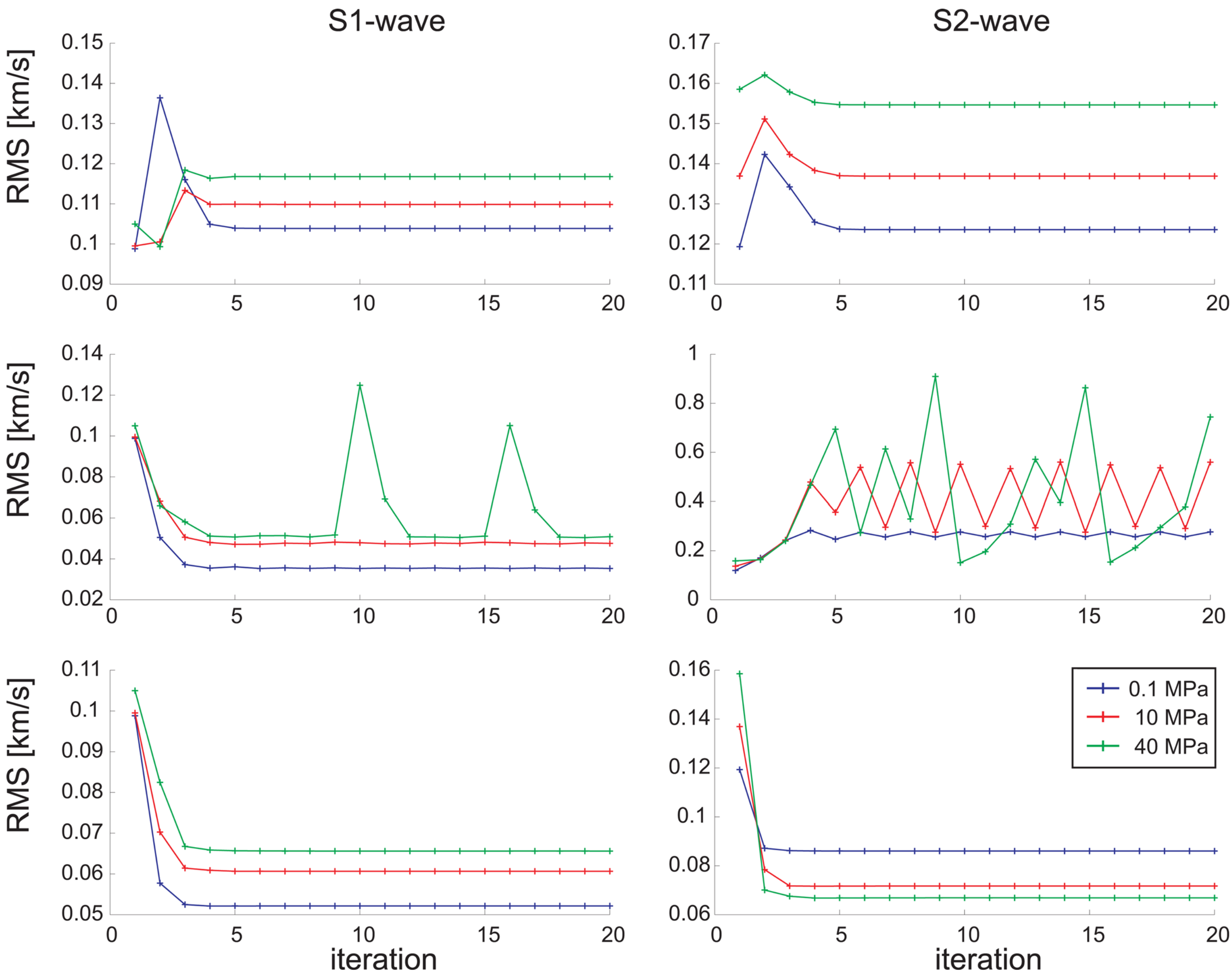

Figure 11. Convergence of iterations of the inversion for three selected confining pressure levels: 0.1 MPa (blue line), 10 MPa (red line) and 40 MPa (green line). Left-hand column: rms of the $S1$-wave velocities, right-hand column: rms of the $S2$-wave velocities, both calculated using three data sets: the P-waves velocities only (top row), the P- and $S1$-wave velocities (middle row), and the P-, $S1$- and $S2$-wave velocities (bottom row).

These plots demonstrate convergence of the iterations. The rms values are calculated as follows:

$$\mathrm{rms}^{S1,S2} = \sqrt{\sum \frac{\left(c_{\mathrm{obs}}^{S1,S2} - c_{\mathrm{pred}}^{S1,S2}\right)^2}{n}}, \tag{10}$$

where $c_{\mathrm{obs}}^{S1,S2}$ are the measured velocities, $c_{\mathrm{pred}}^{S1,S2}$ are the velocities calculated from the retrieved elastic tensor and n is the number of directions in which the velocities are measured. According to the behaviour of the rms values we arrive at the following conclusions:

(1) The calculation based on the 'P-wave velocities only' method produces stable shear velocities which are not further improved through the iterative process. However, the rms value is rather high and mostly unacceptable.

(2) The calculation based on the 'P- and $S1$-wave velocities' method produces oscillations of both predicted S-wave velocities among several velocity models and the rms level is unacceptable as well. The iterative process does not converge even after 20 iterations for some confining pressure values.

(3) Including measurements of the $S2$-wave velocities improves the stability of the iteration process. The predicted shear velocities converge and the rms level reaches the lowest value. The iterative process is robust and converges very quickly.

4.5 Pressure dependence of anisotropy

For distinguishing different origins of anisotropy it is important to analyse elastic properties of the rock sample as a function of confining pressure. With increasing pressure, strength of anisotropy can be changed as well as its symmetry. Since anisotropy of the sample is not weak at some of pressure levels (e.g. P-wave anisotropy is 21.4 per cent at the atmospheric pressure), we cannot simply neglect the differences between the ray and phase velocities. First, the ray velocities must be recalculated to the phase velocities according to Section 2.2 and then inverted according to Section 2.1.

Table 2 summarizes the elastic stiffness coefficients calculated by the iterative inversion from the P- and S-wave velocities measured at pressures of 0.1, 5, 10, 20, 40 and 70 MPa. Fig. 12 presents the calculated P-, $S1$- and $S2$-wave phase velocities from the retrieved elastic parameters of the sample exposed to individual pressure levels. The patterns of the P- and S-wave phase velocities indicate the commonly observed increase of velocities with confining pressure

Table 2. Elastic parameters of rock sample OKU-409 retrieved using measurements of the *P*-, *S*1- and *S*2-wave velocities at six individual levels of confining pressure.

Elastic tensor (GPa)	Pressure (MPa)					
	0.1	5	10	20	40	70
c11	80.3 ± 2.3	83.7 ± 2.0	86.6 ± 1.8	93.7 ± 1.3	96.7 ± 1.5	97.7 ± 1.6
c22	65.1 ± 0.2	70.0 ± 0.4	75.5 ± 0.5	83.0 ± 0.9	86.0 ± 0.8	87.3 ± 0.8
c33	98.3 ± 1.3	98.8 ± 1.3	101.0 ± 1.2	105.3 ± 1.1	107.1 ± 1.0	108.5 ± 1.2
c44	24.6 ± 0.7	24.8 ± 0.7	25.6 ± 0.8	26.8 ± 0.7	27.6 ± 0.8	27.9 ± 0.7
c55	25.8 ± 1.1	26.1 ± 1.1	27.1 ± 1.1	28.2 ± 0.9	29.0 ± 1.0	29.2 ± 1.0
c66	22.4 ± 0.5	22.9 ± 0.5	23.6 ± 0.7	25.0 ± 0.5	25.9 ± 0.7	26.0 ± 0.6
c12	27.1 ± 0.2	30.2 ± 0.4	32.7 ± 0.7	37.7 ± 0.6	38.9 ± 0.9	39.9 ± 0.6
c13	37.3 ± 0.8	37.9 ± 0.7	39.1 ± 0.8	42.7 ± 0.8	43.5 ± 0.7	44.1 ± 0.5
c14	0.3 ± 1.9	0.4 ± 1.5	0.1 ± 0.7	0.1 ± 0.9	−0.1 ± 0.5	−0.1 ± 0.2
c15	−0.7 ± 1.1	−0.6 ± 0.7	−0.3 ± 0.5	−0.4 ± 0.7	−0.4 ± 0.7	−0.6 ± 1.1
c16	2.5 ± 2.4	2.2 ± 2.1	1.8 ± 1.7	1.4 ± 1.6	1.5 ± 1.5	1.5 ± 1.5
c23	31.8 ± 1.3	33.0 ± 1.2	35.0 ± 1.2	38.5 ± 0.8	39.2 ± 1.2	40.2 ± 1.1
c24	0.9 ± 1.7	0.8 ± 1.8	0.5 ± 1.3	0.2 ± 0.9	0.1 ± 0.7	−0.0 ± 0.6
c25	−0.7 ± 1.1	−0.5 ± 0.7	−0.7 ± 0.9	−0.6 ± 0.9	−0.72 ± 1.10	−1.0 ± 1.5
c26	1.9 ± 2.1	1.6 ± 1.7	1.2 ± 1.4	0.8 ± 1.2	1.0 ± 1.3	1.0 ± 1.3
c34	1.9 ± 3.9	1.5 ± 3.0	1.3 ± 2.3	1.1 ± 1.8	0.7 ± 1.2	0.7 ± 1.2
c35	−1.1 ± 1.6	−1.0 ± 1.4	−0.9 ± 1.2	−0.9 ± 1.2	−0.9 ± 1.4	−1.1 ± 1.7
c36	1.6 ± 2.3	1.5 ± 2.1	1.3 ± 1.6	1.0 ± 1.5	1.3 ± 1.5	1.4 ± 1.5
c45	−0.3 ± 0.3	−0.2 ± 0.3	−0.1 ± 0.4	−0.1 ± 0.4	0.0 ± 0.4	0.1 ± 0.4
c46	0.2 ± 0.2	0.1 ± 0.1	0.4 ± 0.3	0.3 ± 0.1	0.2 ± 0.1	0.2 ± 0.2
c56	0.5 ± 0.9	0.1 ± 0.5	−0.02 ± 0.28	−0.0 ± 0.1	−0.1 ± 0.1	−0.0 ± 0.1

pointing to a progressive closure of microcracks (Pros *et al.* 1998; Nadri *et al.* 2011; Piane *et al.* 2011; Lokajíček *et al.* 2013). At pressure of 70 MPa, the effect of microcracks with a low-aspect ratio is minimized and the respective velocity surfaces reflect rather the velocity distribution of the crystallographic-preferred orientation (CPO) anisotropy. Importantly, the nearly orthorhombic symmetry of the velocity patterns observed at low pressures is preserved as pressure is increased. This indicates that crack- and CPO-related fabrics are symmetrically disposed.

Note that a pressure dependence of anisotropy was analysed for the same sample also by Lokajíček *et al.* (2014, their fig. 10). Comparing the predicted phase velocities obtained by both approaches for identical pressure levels (0.1, 20 and 70 MPa), we find that they are slightly different. These inconsistencies are produced by a less accurate inversion applied by Lokajíček *et al.* (2014) in which the differences between the ray and phase velocities were ignored.

5 CONCLUSIONS

The accuracy of the retrieved elastic tensor depends on the following factors:

(1) If only the *P*-wave velocities are measured and inverted for the elastic tensor, some value of the V_P/V_S ratio of the reference isotropic medium must be supplied in the first iteration of the inversion. In next iterations, no such information is needed and the inversion can modify all elastic parameters including those responsible mainly for values of the *S*-wave velocities. Nevertheless, if the starting value is very roughly estimated or completely incorrect, the iteration process does not converge to the true values. In this case, only a part of the elastic tensor is well retrieved and the *S*-wave related parameters C_{44}, C_{45}, C_{46}, C_{55}, C_{56} and C_{66} are inaccurate.

(2) If the *P*- and *S*1-wave velocities are measured and inverted for the elastic tensor, the problem with the artificial value of the V_P/V_S ratio supplied in the first iteration is removed. The synthetic tests show that additional information on the *S*1-wave velocities remarkably increases the accuracy of the inversion and decreases its sensitivity to the starting value of the V_P/V_S ratio. However, if a small number of measurements of the *S*1-wave velocity is included or if the measurements suffer from high picking errors, the fit between the true and predicted *P*-wave velocities can become even worse than if only the accurate *P*-wave velocities are inverted.

(3) If the *P*-, *S*1- and *S*2-wave velocities are available, the inversion results display the highest accuracy. This applies even to the case when the *S*1- and *S*2-wave velocities are measured with a significantly less accuracy than the *P*-wave velocities, for example with the *S*-wave velocity errors of 10–15 per cent compared to the *P*-wave velocity errors of 0.1 per cent. The synthetic tests as well as the processing of real data confirm that the *S*2-wave velocities included into the inversion stabilize the iterative cycle and produce the smallest deviations from observations.

(4) If the *S*1- and *S*2-wave velocities are measured in a small number of directions (6 or 30 directions), the inversion yields results with almost twice higher accuracy for regularly distributed directions than for randomly distributed directions. The more directions are inverted, the higher accuracy of the elastic tensor is obtained. Hence, measurements with a limited number of independent directions are better to carry out in a regular arrangement.

(5) The accuracy of the measured *P*-wave velocities obtained by ultrasonic measurements on spherical samples under confining loading is about 50 m s^{-1}. Based on the rms comparison of the measured and predicted *S*1- and *S*2-wave velocities it is shown that the most accurate elastic parameters are obtained if velocities of all three wave types are inverted. The rms value of real data reached a satisfactory level of 50–70 m s^{-1} and 70–90 m s^{-1} for the *S*1- and *S*2-wave velocities, respectively.

(6) If ray velocities are measured in a lab experiment and strength of anisotropy of a rock is higher than about 10 per cent, we recommend transforming the ray velocities to the phase velocities before the inversion. This transform is rather simple and improves the accuracy of the retrieved anisotropic parameters.

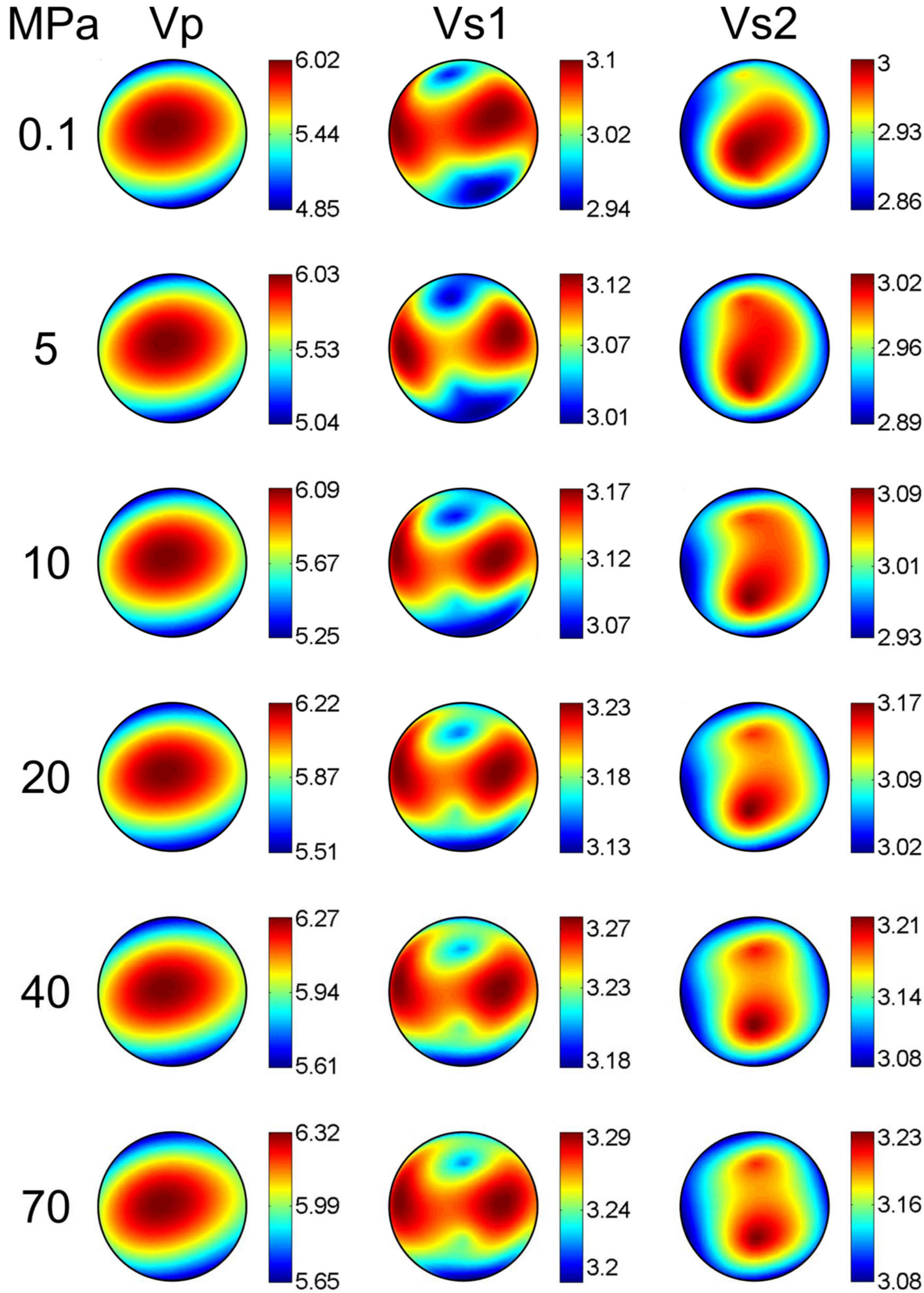

Figure 12. The *P*-, *S*1- and *S*2-wave phase velocities corresponding to the retrieved elastic parameters (see Table 2) under six levels of confining pressure. The colour-coded velocities are in km s^{-1}.

ACKNOWLEDGEMENTS

We wish to thank Andrej Bóna and an anonymous reviewer for their helpful reviews. This study was supported by the Academy of Sciences of the Czech Republic, project RVO 67985831, by the Ministry of Education, project Kontakt II LH13102, and by the Grant Agency of the Czech Republic, projects P104/12/0915, P210/12/1491 and 13–13967S.

REFERENCES

Allen, R., 1982. Automatic phase pickers: their present use and future prospects, *Bull. seism. Soc. Am.,* **72**(6), S225–S242.

Asgharzadeh, M., Bóna, A., Pevzner, V, Urosevic, M. & Gurevich, B., 2013. Reliability of the slowness and slowness-polarization methods for anisotropy estimation in VTI media from 3C walkaway VSP data, *Geophysics,* **78**(5), WC93–WC102.

Bóna, A., Bucataru, I. & Slawinski, M.A., 2008. Inversion of ray velocity and polarization for elasticity tensor, *J. appl. Geophys.,* **65**(1), 1–5.

Bóna, A., Nadri, D. & Brajanovski, M., 2012. Thomsen's parameters from P-wave measurements in a spherical sample, *Geophys. Prospect.,* **60**(1), 103–116.

Červený, V., 2001. *Seismic Ray Theory,* Cambridge Univ. Press.

Christensen, N.I., 1966. Elasticity of ultrabasic rocks, *J. geophys. Res.,* **71**(24), 5921–5931.

Crampin, S., 1985. Evaluation of anisotropy by shear-wave splitting, *Geophysics,* **50**(1), 142–152.

Dewhurst, D.N. & Siggins, A.F., 2006. Impact of fabric, microcracks and stress field on shale anisotropy, *Geophys. J. Int.,* **165**(1), 135–148.

Elbra, T., Karlqvist, R., Lassila, I., Hæggström, E. & Pesonen, L.J., 2011. Laboratory measurements of the seismic velocities and other petrophysical properties of the Outokumpu deep drill core samples, eastern Finland, *Geophys. J. Int.,* **184,** 405–415.

Farra, V. 2004. Improved first-order approximation of group velocities in weakly anisotropic media, *Stud. Geophys. Geod.,* **48,** 199–213.

Helbig, K., 1994. *Foundations of Anisotropy for Exploration Seismics,* Pergamon.

Hornby, B.E., 1998. Experimental laboratory determination of the dynamic elastic properties of wet, drained shales, *J. geophys. Res.,* **103**(B12), 29 945–29 964.

Ildefonse, B., Launeau, P., Bouchez, J.-L. & Fernandez, A. (1992). Effect of mechanical interactions on the development of shape preferred orientations: a two-dimensional experimental approach, *J. Struct. Geol.,* **14**(1), 73–83.

Ivankina, T.I., Kern, H.M. & Nikitin, A.N., 2005. Directional dependence of P- and S-wave propagation and polarization in foliated rocks from the Kola superdeep well: evidence from laboratory measurements and calculations based on TOF neutron diffraction, *Tectonophysics,* **407**(1–2), 25–42.

Jech, J., 1991. Computation of elastic parameters of anisotropic medium from travel times of quasi-compressional waves, *Phys. Earth planet. Inter.,* **66**(3–4), 153–159.

Jech, J. & Pšenčík, I., 1989. First-order perturbation method for anisotropic media, *Geophys. J. Int.,* **99,** 369–376.

Karato, S., 2008. *An Introduction to Rheology of Solid Earth,* Cambridge Univ. Press.

Kern, H., 1982. Elastic-wave velocity in crustal and mantle rocks at high pressure and temperature: the role of the high-low quartz transition and of dehydration reactions, *Phys. Earth planet. Inter.,* **29**(1), 12–23.

Kern, H., Ivankina, T.I., Nikitin, A.N., Lokajíček, T. & Pros, Z., 2008. The effect of oriented microcracks and crystallographic and shape preferred orientation on bulk elastic anisotropy of a foliated biotite gneiss from Outokumpu, *Tectonophysics,* **457**(3–4), 143–149.

Kern, H., Mengel, K., Strauss, K.W., Ivankina, T.I., Nikitin, A.N. & Kukkonen, I.T., 2009. Elastic wave velocities, chemistry and modal mineralogy of crustal rocks sampled by the Outokumpu scientific drill hole: evidence from lab measurements and modeling, *Phys. Earth planet. Inter.,* **175**(3–4), 151–166.

Kitamura, K., 2006. Constraint of lattice-preferred orientation (LPO) on Vp anisotropy of amphibole-rich rocks, *Geophys. J. Int.,* **165**(3), 1058–1065.

Klíma, K., 1973. The computation of the elastic constants of an anisotropic medium from the velocities of body waves, *Stud. Geophys. Geod.,* **17**(2), 115–122.

Kukkonen, I.T., Rath, V., Kivekas, L., Šafanda, J. & Čermák, V., 2011. Geothermal studies of the Outokumpu Deep Drill Hole, Finland: vertical variation in heat flow and palaeoclimatic implications, *Phys. Earth planet. Int.,* **188,** 9–25.

Lipschutz, S., 1969. *Theory and Problems of Differential Geometry,* McGraw-Hill.

Lokajíček, T. & Klíma, K., 2006. A first arrival identification system of acoustic emission (AE) signals by means of a high-order statistics approach, *Measur. Sci. Technol.,* **17**(9), 2461–2466.

Lokajíček, T., Goel, R.K., Rudajev, V. & Dwivedi, R.D., 2013. Assessment of velocity anisotropy in rocks, *Int. J. Rock Mech. Min. Sci.,* **57,** 142–152.

Lokajíček, T., Kern, H., Svitek, T. & Ivankina, T., 2014. 3D velocity distribution of P- and S-waves in a biotite gneiss, measured in oil as the pressure medium: comparison with velocity measurements in a multi-anvil pressure apparatus and with texture-based calculated data, *Phys. Earth planet. Inter.,* **231,** 1–15.

Mainprice, D. & Nicolas, A., 1989. Development of shape and lattice preferred orientations: application to the seismic anisotropy of the lower crust, *J. Struct. Geol.,* **11**(1), 175–189.

Mensch, T. & Rasolofosaon, P., 1997. Elastic-wave velocities in anisotropic media of arbitrary symmetry—generalization of Thomsen's parameters ε, δ and γ, *Geophys. J. Int.,* **128,** 43–63.

Musgrave, M.J.P., 1970. *Crystal Acoustics,* Holden-Day.

Nadri, D., Bona, A., Brajanovski, M. & Lokajíček, T., 2011. Estimation of stress-dependent anisotropy from P-wave measurements on a spherical sample, *Geophysics,* **76**(3), WA91–WA100.

Nikitin, A.N. & Ivankina, T.I., 2004. Neutron diffractometry in geosciences, *Phys. Particle Nucl.,* **35**(2), 193–224.

Okaya, D., Rabbel, W., Beilecke, T. & Hasenclever, J., 2004. P wave material anisotropy of tectono-metaorphic terrane: an active source seismic experiment at the KTB super-deep drill hole, southeast Germany, *Geophys. Res. Lett.,* **31,** L24620, doi:10.1029/2004GL020855.

Peng, Z. & Ben-Zion, Y., 2004. Systematic analysis of crustal anisotropy along the Karadere-Düzce branch of the north Anatolian fault, *Geophys. J. Int.,* **159,** 253–274.

Piane, C.D., Dewhurst, D.N., Siggins, A.F. & Raven, M.D., 2011. Stress-induced anisotropy in brine saturated shale, *Geophys. J. Int.,* **184**(2), 897–906.

Pros, Z., Lokajíček, T. & Klíma, K., 1998. Laboratory approach to the study of elastic anisotropy on rock samples, *Pure Appl. Geophys.,* **151**(2–4), 619–629.

Pšenčík, I. & Gajewski, D., 1998. Polarization, phase velocity and NMO velocity of qP waves in arbitrary weakly anisotropic media, *Geophysics,* **63,** 1754–1766.

Pšenčík, I. & Vavryčuk, V., 2002. Approximate relation between the ray vector and wave normal in weakly anisotropic media, *Stud. Geophys. Geod.,* **46,** 793–807.

Savage, M.K., 1999. Seismic anisotropy and mantle deformation: What have we learned from shear wave splitting?, *Rev. Geophysics,* **37,** 65–106.

Sayers, C.M., 2002. Fluid-dependent shear-wave splitting in fractured media, *Geophys. Prospect.,* **50**(4), 393–401.

Sayers, C.M. & Kachanov, M., 1995. Microcrack-induced elastic-wave anisotropy of brittle rocks, *J. geophys. Res.,* **100**(B3), 4149–4156.

Sedlák, P., Hirose, Y., Khan, S.A., Enoki, M. & Sikula, J., 2009. New automatic localization technique of acoustic emission signals in thin metal plates, *Ultrasonics,* **49**(2), 254–262.

Siegesmund, S., Kern, H. & Vollbrecht, A., 1991. The effect of oriented microcracks on seismic velocities in an ultramylonite, *Tectonophysics,* **186**(3–4), 241–251.

Svitek, T., Rudajev, V. & Petružálek, M., 2010. Determination of P–wave arrival time of acoustic events, *Acta Montan. Slov.,* **15**(2), 145–151.

Valcke, S.L.A., Casey, M., Lloyd, G.E., Kendall, J.-M. & Fisher, Q.J., 2006. Lattice preferred orientation and seismic anisotropy in sedimentary rocks, *Geophys. J. Int.,* **166**(2), 652–666.

Vavryčuk, V., 1997. Elastodynamic and elastostatic Green tensors for homogeneous weak transversely isotropic media, *Geophys. J. Int.,* **130,** 786–800.

Vavryčuk, V., 2005a. Acoustic axes in triclinic anisotropy, *J. Acoust. Soc. Am.,* **118,** 647–653.

Vavryčuk, V., 2005b. Acoustic axes in weak triclinic anisotropy, *Geophys. J. Int.,* **163,** 629–638.

Vavryčuk, V., 2006. Calculation of the slowness vector from the ray vector in anisotropic media, *Proc. Roy. Soc. A,* **462,** 883–896.

Vavryčuk, V., 2009. Weak anisotropy-attenuation parameters, *Geophysics,* **74**(5), WB203–WB213.

Vavryčuk, V., 2013. Inversion for weak triclinic anisotropy from acoustic axes, *Wave Motion,* **50**(8), 1271–1282.

Wang, X.-Q., Schubnel, A., Fortin, J., David, E.C., Guéguen, Y. & Ge, H.-K., 2012. High Vp/Vs ratio: Saturated cracks or anisotropy effects?, *Geophys. Res. Lett.,* **39**(11), L11307, doi:10.1029/2012GL051742.

Wenk, H.-R., Vasin, R.N., Kern, H., Matthies, S., Vogel, S.C. & Ivankina, T.I., 2012. Revisiting elastic anisotropy of biotite gneiss from the Outokumpu scientific drill hole based on new texture measurements and texture-based velocity calculations, *Tetonophysics,* **570–571,** 123–134.

Xie, Y., Wenk, H.-R. & Matthies, S., 2003. Plagioclase preferred orientation by TOF neutron diffraction and SEM-EBSD, *Tectonophysics,* **370**(1–4), 269–286.